Finite-size scaling and multifractality at the Anderson transition for the three Wigner-Dyson symmetry classes in three dimensions

László Ujfalusi* and Imre Varga†

Elméleti Fizika Tanszék, Fizikai Intézet, Budapesti Műszaki és Gazdaságtudományi Egyetem, H-1521 Budapest, Hungary

(Received 9 January 2015; revised manuscript received 1 May 2015; published 26 May 2015)

The disorder-induced metal-insulator transition is investigated in a three-dimensional simple cubic lattice and compared for the presence and absence of time-reversal and spin-rotational symmetry, i.e., in the three conventional symmetry classes. Large-scale numerical simulations have been performed on systems with linear sizes up to $L = 100$ in order to obtain eigenstates at the band center, $E = 0$. The multifractal dimensions, exponents D_q and α_q, have been determined in the range of $-1 \leqslant q \leqslant 2$. The finite-size scaling of the generalized multifractal exponents provide the critical exponents for the different symmetry classes in accordance with values known from the literature based on high-precision transfer matrix techniques. The multifractal exponents of the different symmetry classes provide further characterization of the Anderson transition, which was missing from the literature so far.

DOI: 10.1103/PhysRevB.91.184206 PACS number(s): 71.23.An, 71.30.+h, 72.15.Rn

I. INTRODUCTION

The metal-insulator transition (MIT) and disordered systems have been at the forefront of condensed matter research since the middle of the last century [1], and yet this topic still has several open questions and is still actively investigated. In the last few years experimental evidence has been obtained about this topic; in particular, reporting Anderson localization of ultrasound in disordered elastic networks [2,3], or light in disordered photonic lattices in the transverse direction [4] or in an ultracold atomic system in a disordered laser trap [5]. Richardella *et al.* [6] examined the MIT in a dilute magnetic semiconductor $Ga_{1-x}Mn_xAs$, which is a strongly interacting and disordered system. They found a clear phase transition together with multifractal fluctuations of the local density of states (LDOS) at the Fermi energy, showing that multifractality is a robust and important property of disordered systems. Multifractal properties consistent with the theory of Anderson localization are also found in the ultrasound system [3]. On the theoretical side, we know that disorder plays a crucial role in integer quantum Hall effect [7], and recently it was shown that an enhanced correlation of multifractal wave-function densities in disordered systems can increase the superconducting critical temperature [8] or the multifractal fluctuations of the LDOS close to criticality may lead to a new phase due to the presence of local Kondo effects induced by local pseudogaps at the Fermi energy [9]. Moreover, Anderson localization has also been reported in the spectrum of the Dirac operator within the lattice model of QCD at high temperatures using spectral statistics [10], and multifractal analysis seems to corroborate it as well [11].

These models show an increased interest in understanding the nature of the Anderson transition in the presence of various global symmetries. A comprehensive review of the current understanding is given in Ref. [12]. These symmetry classes have been introduced first to describe random matrix ensembles, but the naming conventions are the same in the field of disordered systems. The classification considers two global symmetries: time-reversal and spin-rotational symmetry. As it turns out, beside these symmetries there are three further symmetry classes according to the presence of chiral symmetry, and in addition there are four Bogoliubov-de Gennes classes also, corresponding to particle-hole symmetry [12] prominent in hybrid (superconductor-normal) systems. The effect of symmetry classes at the Anderson transition has already been investigated earlier [13] using spectral statistics, but there is much less work based on the multifractal analysis of the eigenstates, and multifractal exponents are known numerically only for the orthogonal class [14].

Our goal in this article is to fill in this gap and apply multifractal finite-size scaling (MFSS), developed originally by Rodriguez, Vasquez, Römer, and Slevin [14], to the Anderson models in the three conventional Wigner-Dyson (WD) classes. The organization of the article is the following: In Sec. II we define the model and describe its numerical representation. In Sec. III we briefly describe the finite-size scaling analysis of the generalized multifractal exponents of the critical eigenstates, in Sec. IV we give the results obtained for the three universality classes and finally in Sec. V we summarize our results.

II. MODELS AND NUMERICAL REPRESENTATION

A. The model

In this article we investigate Anderson models belonging to the three WD classes, without chiral and particle-hole symmetry. We investigate the case of diagonal disorder and nearest-neighbor hopping; therefore, the Hamiltonian reads

$$\mathcal{H} = \sum_{i\sigma} \varepsilon_i c^\dagger_{i\sigma} c_{i\sigma} - \sum_{ij\sigma\sigma'} t_{ij\sigma\sigma'} c^\dagger_{i\sigma} c_{j\sigma'} + \text{H.c.}, \qquad (1)$$

where i, j and σ,σ' stand for site and spin index, ε_i are random on-site energies, which are uniformly distributed over the interval $[-\frac{W}{2}, \frac{W}{2}]$, W acts as disorder strength. Using a uniform distribution is just a convention, other distributions of disorder, e.g., Gaussian, binary, etc. can be used as well.

*ujfalusi@phy.bme.hu
†varga@phy.bme.hu

In the orthogonal class time-reversal and spin-rotational symmetry are preserved. In this case the Hamiltonian is invariant under orthogonal transformations—hence the name—therefore it is a real symmetric matrix. Since spin does not play a role, we consider a spinless Anderson model. In the numerical simulations the Hamiltonian is represented by an $N \times N$ real symmetric matrix, where $N = L^3$, and L is the linear system size in lattice spacing. The diagonal elements are are uniformly distributed random numbers, the off-diagonal elements are zero, except if i and j are nearest neighbors:

$$H_{ij}^{O} = \begin{cases} \varepsilon_i \in U\left[-\frac{W}{2}, \frac{W}{2}\right], \text{if } i = j \\ -1, \text{if } i \text{ and } j \text{ are neighboring sites} \\ 0, \text{otherwise.} \end{cases} \quad (2)$$

The energy unit is fixed by setting the hopping elements to 1. To avoid surface effects, we use periodic boundary conditions. However, this case was investigated very carefully by Rodriguez *et al.* [14]; we consider this symmetry class to verify our numerical method and to obtain a complete description of all the WD classes.

In the unitary class time-reversal symmetry is broken, which can be realized physically by applying a magnetic field. It can be shown that either spin rotational symmetry is broken or not, the model will belong to the unitary class [12]. The Hamiltonian is invariant under unitary transformations, therefore it is a complex Hermitian matrix. We discuss the case when spin-rotational symmetry is present, because this way we can use spinless fermions again, which keeps the matrix size $N \times N$. However, one has to store about twice as much data compared with the orthogonal case, because here every off-diagonal matrix element is a complex number. Obviously, finding an eigenvalue and an eigenvector takes more time, too.

For the numerical simulations we followed Slevin and Ohtsuki [15]. Let us consider a magnetic field pointing in the y direction with flux Φ, measured in units of the flux quantum, h/e. Its effect can be represented by a unity phase factor, the Peierls substitution for the hopping elements of the Hamiltonian matrix. The upper triangular of the Hamiltonian reads

$$H_{i\leqslant j}^{U} = \begin{cases} \varepsilon_i \in U\left[-\frac{W}{2}, \frac{W}{2}\right], \text{if } i = j \\ -1, \text{if } i \text{ and } j \text{ are neighboring sites} \\ \quad \text{in the } x \text{ or } y \text{ direction} \\ -e^{i2\pi\Phi x}, \text{if } i \text{ and } j \text{ are neighboring} \\ \quad \text{sites in the } z \text{ direction} \\ 0, \text{otherwise.} \end{cases} \quad (3)$$

Complex Hermiticity sets the off-diagonal elements in the lower triangular part, $j < i$. Periodic boundary conditions and flux quantization force a restriction for the magnetic flux; namely, that $\Phi \cdot L$ must be an integer. In the thermodynamic limit, arbitrarily small magnetic field drives the system from the orthogonal to the unitary class. However, in a finite system the relationship between the system size L and the magnetic length, $L_H = \frac{1}{\sqrt{2\pi\Phi}}$, matters. In the case of weak magnetic field, $L \ll L_H$, the system belongs to the orthogonal class, in the case of strong magnetic field, $L \gg L_H$, it belongs to the unitary class. Since we use system sizes that are multiples of ten lattice spacings, see Table I, we chose $\Phi = \frac{1}{5}$. This leads to $L_H \approx 0.892$; therefore, this choice clearly fulfills the two conditions above.

TABLE I. System sizes and number of samples for the simulation for each WD symmetry class.

System size (L)	Number of samples
20	15 000
30	15 000
40	15 000
50	15 000
60	10 000
70	7500
80	5000
90	4000
100	3500

In the symplectic class time-reversal symmetry is present, and spin-rotational symmetry is broken, which describes a system with spin-orbit interaction. In this case the Hamiltonian is invariant under symplectic transformations; therefore, it is a quaternion Hermitian matrix. For the numerical simulations we followed Asada, Slevin, and Ohtsuki [16]. Since in this case we have to deal with the spin index also, the Hamiltonian is an $2N \times 2N$ complex Hermitian matrix. Diagonal elements corresponding to the ith site and hopping elements between sites i and j are 2×2 matrices because of the spin indexes, having a form

$$\epsilon_i = \begin{pmatrix} \varepsilon_i & 0 \\ 0 & \varepsilon_i \end{pmatrix}, \quad t_{ij} = \begin{pmatrix} e^{i\alpha_{ij}\cos\beta_{ij}} & e^{i\gamma_{ij}\sin\beta_{ij}} \\ -e^{-i\gamma_{ij}\sin\beta_{ij}} & e^{-i\alpha_{ij}\cos\beta_{ij}} \end{pmatrix}, \quad (4)$$

where ε_i is an uniformly distributed random on-site energy from the interval $[-\frac{W}{2}, \frac{W}{2}]$, α_{ij}, β_{ij}, and γ_{ij} were chosen to form an SU(2)-invariant parametrization, leading to the so-called SU(2) model: α_{ij} and γ_{ij} are uniform random variables from the interval $[0, 2\pi]$, and β has a probability density function $p(\beta)d\beta = \sin(2\beta)d\beta$ in the range $[0, \frac{\pi}{2}]$. The upper triangular of the Hamiltonian has the following form:

$$H_{i\leqslant j}^{S} = \begin{cases} \epsilon_i, \text{if } i = j \\ t_{ij}, \text{if } i \text{ and } j \text{ are neighboring sites} \\ 0, \text{otherwise.} \end{cases} \quad (5)$$

The off-diagonal elements are defined following complex Hermiticity. To store the Hamiltonian requires about eight times more memory compared to the orthogonal case, because here every off-diagonal element contains four complex numbers. Finding an eigenvalue is much slower than for the unitary case, mainly because of the linear size of the matrix is twice as large.

B. Numerical method

MFSS deals with the eigenvectors of the Hamiltonian, which is a large sparse matrix. Recent high-precision calculations [14] use Jacobi-Davidson iteration with incomplete LU preconditioning; therefore we decided to use this combination. For preconditioning ILUPACK [17] was used, for the JD iteration the PRIMME [18] package was used. Since the metal-insulator transition occurs at the band center [12] ($E = 0$) at disorder $W_c^O \approx 16.5$ for the orthogonal, at $W_c^U \approx 18.3$ for the unitary

(depending on the strength of magnetic field), at $W_c^S \approx 20$ for the symplectic class (for our parameters), most works study the vicinity of these points. To have the best comparison, we analyzed this regime, therefore 20 disorder values were taken from the range $15 \leqslant W \leqslant 18$ for the orthogonal class, 23 disorder values were taken from the interval $17 \leqslant W \leqslant 20$ for the unitary class, and 20 disorder values were taken from the interval $19.4 \leqslant W \leqslant 20.5$ for the symplectic class. System sizes were taken from the range $L = 20..100$, and the number of samples are listed in Table I. We considered only one wave function per realization, the one with energy closest to zero in order to avoid correlations between wave functions of the same system [14].

III. FINITE-SIZE SCALING LAWS FOR GENERALIZED MULTIFRACTAL EXPONENTS

In recent high-precision calculations [14] the multifractal exponents (MFEs) of the eigenfunctions of the Hamiltonian have been used to describe the Anderson metal-insulator transition. We use almost the same notation and methods as Ref. [14], but for better understanding here we introduce shortly the most important quantities and notations. The method has recently been successfully extended for the investigation of the quantum percolation transition in three dimensions [19].

Considering a d-dimensional cubic lattice with linear size L, one can divide this lattice into smaller boxes with linear size ℓ. If Ψ is an eigenfunction of the Hamiltonian, the probability corresponding to the kth box reads

$$\mu_k = \sum_{i \in \mathrm{box}_k} |\Psi_i|^2. \tag{6}$$

One can introduce the qth moment of the box probability (frequently called generalized inverse participation ratio, GIPR), and its derivative:

$$R_q = \sum_{k=1}^{\lambda^{-d}} \mu_k^q, \quad S_q = \frac{dR_q}{dq} = \sum_{k=1}^{\lambda^{-d}} \mu_k^q \ln \mu_k. \tag{7}$$

The average of R_q and S_q follows a power-law behavior as a function of $\lambda = \frac{\ell}{L}$, with exponent τ_q and α_q:

$$\tau_q = \lim_{\lambda \to 0} \frac{\ln \langle R_q \rangle}{\ln \lambda}, \quad \alpha_q = \frac{d\tau_q}{dq} = \lim_{\lambda \to 0} \frac{\langle S_q \rangle}{\langle R_q \rangle \ln \lambda}. \tag{8}$$

τ_q can be rewritten in the following form:

$$\tau_q = D_q(q-1) = d(q-1) + \Delta_q, \tag{9}$$

where D_q is the generalized fractal dimension, and Δ_q is the anomalous scaling exponent. Employing a Legendre transform on τ_q, we obtain the singularity spectrum $f(\alpha)$:

$$f(\alpha_q) = q\alpha_q - \tau_q. \tag{10}$$

τ_q, α_q, D_q, and Δ_q are often referred to as multifractal exponents.

According to recent results [20] a symmetry relation exists for α_q and Δ_q given in the form:

$$\Delta_q = \Delta_{1-q}, \quad \alpha_q + \alpha_{1-q} = 2d. \tag{11}$$

For numerical approaches one has to define the finite-size version of these MFEs at a particular value of disorder:

$$\tilde{\alpha}_q^{\mathrm{ens}}(W,L,\ell) = \frac{\langle S_q \rangle}{\langle R_q \rangle \ln \lambda}, \tag{12}$$

$$\tilde{D}_q^{\mathrm{ens}}(W,L,\ell) = \frac{1}{q-1} \frac{\ln \langle R_q \rangle}{\ln \lambda}, \tag{13}$$

where *ens* stands for *ensemble* averaging over the different disorder realizations. One may define *typical* averaged versions also:

$$\tilde{\alpha}_q^{\mathrm{typ}}(W,L,\ell) = \left\langle \frac{S_q}{R_q} \right\rangle \frac{1}{\ln \lambda}, \tag{14}$$

$$\tilde{D}_q^{\mathrm{typ}}(W,L,\ell) = \frac{1}{q-1} \frac{\langle \ln R_q \rangle}{\ln \lambda}. \tag{15}$$

Similarly to $\tilde{\alpha}_q$ and $\tilde{D}_q$, $\tilde{\Delta}_q$ or $\tilde{\tau}_q$ can be defined, which are called generalized multifractal exponents (GMFEs). Every GMFE approaches the value of the corresponding MFE at the critical point, $W = W_c$, only in the limit $\lambda \to 0$. We would like to emphasize that MFEs are defined through *ensemble* averaging in principle [see Eq. (8)], and *ensemble* and *typical* averaged MFEs are equal only in a range of q, $q_- < q < q_+$ [12], defined by the two zeros of the singularity spectrum, $f(\alpha_{q_-}) = f(\alpha_{q_+}) = 0$. Therefore when in Sec. IV B we compute MFEs, we will use *ensemble* averaged quantities only.

The choice of the investigated range of q is influenced by the following three effects: If q is large, the qth power in Eq. (7) enhances the numerical and statistical errors, leading to a noisy dataset. If q is negative with large absolute value, the relatively less precise small wave-function values dominate the sums in Eq. (7), which also results in a noisy dataset. These two effects together lead to a regime $q_{\min} \leqslant q \leqslant q_{\max}$, where GMFEs behave numerically the best. The third effect is coarse graining which suppresses the noise. For $\ell > 1$ in an $\ell \times \ell \times \ell$-sized box positive and negative errors on the wave functions can cancel each other. Moreover, in a box, large and small wave-function amplitudes appear together with high probability, and this way the relative error of a μ_k box probability is reduced. In other words coarse graining has a nice smoothing effect, which can help to widen the range of q that can be investigated.

The renormalization flow of the AMIT has three fixed points: a metallic, an insulating, and a critical one. In the metallic fixed point every state is extended with probability one; therefore, the effective size of the states grows proportional to the volume, leading to $D_q^{\mathrm{met}} \equiv d$. In the insulating fixed point every state is exponentially localized, the effective size of a state does not change with changing system size, resulting in $D_q^{\mathrm{ins}} \equiv 0$ for $q > 0$, and $D_q^{\mathrm{ins}} \equiv \infty$ for $q < 0$. Renormalization does not change the system at criticality, therefore it is scale independent, which means self-similarity. Therefore, wave functions are supposed to be multifractals; in other words, generalized fractals [21].

Close to the critical point due to standard finite-size scaling arguments one can derive the following scaling laws for the

exponents $\tilde{\alpha}_q$ and $\tilde{D}_q$ defined above:

$$\tilde{\alpha}_q(W,L,\ell) = \alpha_q + \frac{1}{\ln\lambda}\mathcal{A}_q\left(\frac{L}{\xi},\frac{\ell}{\xi}\right), \tag{16a}$$

$$\tilde{D}_q(W,L,\ell) = D_q + \frac{q}{\ln\lambda}\mathcal{T}_q\left(\frac{L}{\xi},\frac{\ell}{\xi}\right). \tag{16b}$$

Equations (16) can be summarized in one equation:

$$\tilde{G}_q(W,L,\ell) = G_q + \frac{1}{\ln\lambda}\mathcal{G}_q\left(\frac{L}{\xi},\frac{\ell}{\xi}\right). \tag{17}$$

(L,ℓ) on the left-hand side and $(\frac{L}{\xi},\frac{\ell}{\xi})$ on the right-hand side can be changed to (L,λ) and $(\frac{L}{\xi},\lambda)$:

$$\tilde{G}_q(W,L,\lambda) = G_q + \frac{1}{\ln\lambda}\mathcal{G}_q\left(\frac{L}{\xi},\lambda\right). \tag{18}$$

Our central goal is to fit the above formulas to the numerically obtained data, where W_c, ν, y, and G_q appear among the fit parameters. This fit procedure will provide us the physically interesting quantities and their confidence intervals. In the next sections we present different methods for the finite-size scaling.

A. Finite-size scaling at fixed λ

At fixed λ, G_q in Eq. (18) can be considered as the constant term of $\mathcal{G}_q$; therefore,

$$\tilde{G}_q(W,L) = \mathcal{G}_q\left(\frac{L}{\xi}\right), \tag{19}$$

where the constant λ has been dropped. $\mathcal{G}_q$ can be expanded with one relevant $[\varrho(w)]$ and one irrelevant $[\eta(w)]$ operator the following way by using $w = W - W_c$:

$$\mathcal{G}_q\left(\varrho L^{\frac{1}{\nu}},\eta L^{-y}\right) = \mathcal{G}_q^r\left(\varrho L^{\frac{1}{\nu}}\right) + \eta L^{-y}\mathcal{G}_q^{ir}\left(\varrho L^{\frac{1}{\nu}}\right). \tag{20}$$

All the disorder-dependent quantities in the above formula can be expanded in Taylor series:

$$\mathcal{G}_q^r\left(\varrho L^{\frac{1}{\nu}}\right) = \sum_{i=0}^{n_r} a_i\left(\varrho L^{\frac{1}{\nu}}\right)^i, \tag{21}$$

$$\mathcal{G}_q^{ir}\left(\varrho L^{\frac{1}{\nu}}\right) = \sum_{i=0}^{n_{ir}} b_i\left(\varrho L^{\frac{1}{\nu}}\right)^i, \tag{22}$$

$$\varrho(w) = w + \sum_{i=2}^{n_\varrho} c_i w^i, \quad \eta(w) = 1 + \sum_{i=1}^{n_\eta} d_i w^i. \tag{23}$$

The advantage of this method is that, in the Taylor series, only one variable appears, $\varrho L^{\frac{1}{\nu}}$, so the number of parameters (including W_c, ν, and y) is $n_r + n_{ir} + n_\rho + n_\eta + 4$, which grows linearly with the expansion orders. This method is very effective for computing W_c, ν, and y, but since λ is fixed, one cannot obtain the MFEs. In all cases we used $\lambda = 0.1$, because it leads to excellent results in Ref. [14]. It seems that it is small enough to capture the details of a wave function, and it allows many different system sizes in the range of $20 \leqslant L \leqslant 100$, which we investigated. This way we can also compare our results to those of Ref. [14] very well.

B. Finite-size scaling for varying λ

In order to take into account different values of λ, the scaling law given in Eq. (17) has to be considered. The expansion of $\mathcal{G}$ in (17) is

$$\begin{aligned}\mathcal{G}_q\left(\varrho L^{\frac{1}{\nu}},\varrho\ell^{\frac{1}{\nu}},\eta' L^{-y'},\eta\ell^{-y}\right) = {}& \mathcal{G}_q^r\left(\varrho L^{\frac{1}{\nu}},\varrho\ell^{\frac{1}{\nu}}\right)\\ &+ \eta' L^{-y'}\mathcal{G}_q'^{ir}\left(\varrho L^{\frac{1}{\nu}},\varrho\ell^{\frac{1}{\nu}}\right)\\ &+ \eta\ell^{-y}\mathcal{G}_q^{ir}\left(\varrho L^{\frac{1}{\nu}},\varrho\ell^{\frac{1}{\nu}}\right).\end{aligned}$$

According to Rodriguez *et al.* [14] the most important irrelevant term is the one containing the finite box size ℓ; therefore, we took into account that one only. This leads to

$$\begin{aligned}\tilde{G}_q(W,L,\ell) = G_q + \frac{1}{\ln\lambda}\big[&\mathcal{G}_q^r\left(\varrho L^{\frac{1}{\nu}},\varrho\ell^{\frac{1}{\nu}}\right)\\ &+,\eta\ell^{-y}\mathcal{G}_q^{ir}\left(\varrho L^{\frac{1}{\nu}},\varrho\ell^{\frac{1}{\nu}}\right)\big].\end{aligned} \tag{24}$$

The Taylor expansions of the above functions are

$$\mathcal{G}_q^r\left(\varrho L^{\frac{1}{\nu}},\varrho\ell^{\frac{1}{\nu}}\right) = \sum_{i=0}^{n_r}\sum_{j=0}^{i} a_{ij}\varrho^i L^{\frac{j}{\nu}}\ell^{\frac{i-j}{\nu}}, \tag{25}$$

$$\mathcal{G}_q^{ir}\left(\varrho L^{\frac{1}{\nu}},\varrho\ell^{\frac{1}{\nu}}\right) = \sum_{i=0}^{n_{ir}}\sum_{j=0}^{i} b_{ij}\varrho^i L^{\frac{j}{\nu}}\ell^{\frac{i-j}{\nu}}, \tag{26}$$

$$\varrho(w) = w + \sum_{i=2}^{n_\varrho} c_i w^i, \quad \eta(w) = 1 + \sum_{i=1}^{n_\eta} d_i w^i. \tag{27}$$

The advantage of this method is that it provides the MFE, G_q, since it is one of the parameters to fit. There are many more data to fit compared to the fixed-λ case. Fixed λ means that, at a given system size, one can use GMFEs obtained at a certain value of ℓ—the one that leads to the desired λ—while in this case one can fit to GMFEs obtained at different values of ℓ. However, these GMFEs are correlated, because they are the results of the coarse graining of the same wave functions with different sizes of boxes. During the fitting procedure one has to take into account these correlations; see Sec. III C. Since the relevant and irrelevant scaling functions have two variables, $\varrho L^{\frac{1}{\nu}}$ and $\varrho\ell^{\frac{1}{\nu}}$, one has to fit a two-variable function with the number of parameters $(n_r+1)(n_r+2)/2 + (n_{ir}+1)(n_{ir}+2)/2 + n_\rho + n_\eta + 3$. We can see that the number of parameters grows as $\sim n_{r/ir}^2$ instead of as $\sim n_{r/ir}$ as for fixed λ. This makes the fitting procedure incorporating the correlations definitely much more difficult.

C. General principles for the finite-size-scaling fit procedures

In this section we discuss the details of the methods and criteria we used during the MFSS. In order to fit the scaling law of Eqs. (19) and (24) we used the MINUIT library [22]. To find the best fit to the data obtained numerically, the order of expansion of $\mathcal{G}_q^{r/ir}$, ϱ and η, must be decided by choosing the values of n_r, n_{ir}, n_ϱ, and n_η. Since the relevant operator is more important than the irrelevant one we always used $n_{\rm rel} \geqslant n_{ir}$ and $n_\varrho \geqslant n_\eta$. To choose the order of the expansion

we used basically three criteria: The first criterion we took into account was to check how close the ratio $\chi^2/(N_{df}-1)$ approached unity, where N_{df} stands for the number of degrees of freedom. Let us denote the numerically obtained data points by y_i, the fit function value at the ith parameter value by f_i, and the correlation matrix of the numerically obtained data points by C, which can be computed numerically with a similar expression to the variance. With these notations, χ^2 reads

$$\chi^2 = \sum_{i,j}(y_i - f_i)(C^{-1})_{ij}(y_j - f_j); \tag{28}$$

for more details see Ref. [14]. If the data points are not correlated, C is a diagonal matrix, and the expression leads to the usual form

$$\chi^2 = \sum_i \frac{(y_i - f_i)^2}{\sigma_i^2}. \tag{29}$$

The number of degrees of freedom, N_{df}, is the number of data points minus the number of fit parameters. A ratio $\chi^2/(N_{df}-1) \approx 1$ means that the deviations from the best fit are of the order of the standard deviation (correlation matrix). The second criterion was that the fit has to be stable against changing the expansion orders, i.e., adding a few new expansion terms. From the fits that fulfilled the first two criteria we chose the simplest model with the lowest expansion orders. Sometimes we also took into account the error bars, and we chose the model with the lowest error bar for the most important quantities (W_c, ν, etc.), if similar models fulfilled the first two criteria.

The error bars of the best fit parameters were obtained by a Monte Carlo simulation. The data points are results of averaging so, due to the central limit theorem, they have a Gaussian distribution. Therefore, we generated Gaussian random numbers with parameters corresponding to the mean of the raw data points and standard deviation (or correlation matrix) of the mean, and then found the best fit. Repeating this procedure $N_{\mathrm{MC}} = 100$ times provided the distribution of the fit parameters. We chose 95% confidence level to obtain the error bars.

IV. RESULTS OF MULTIFRACTAL FINITE-SIZE SCALING FOR ANDERSON MODELS IN WIGNER-DYSON SYMMETRY CLASSES

With the numerical method described in Sec. II we computed an eigenvector for every disorder realization of the Hamiltonian. From the eigenvectors, every GMFE is computable for the orthogonal and unitary class the $|\Psi_i|^2$ expression in Eq. (6) is trivial, and it means summation for the spin index for the symplectic class, since spatial behavior is in our interest. At fixed q exponents τ_q and Δ_q are linear transforms of D_q, so we used only the $\tilde{\alpha_q}$ and $\tilde{D}_q$ GMFEs for the MFSS. We investigate the range $-1 \leqslant q \leqslant 2$, because GMFEs behave the best in this regime for the reasons described in Sec. III.

A. Results of multifractal finite-size scaling at fixed $\lambda = 0.1$

The typical behavior of the GMFEs is presented in Fig. 1. In all cases there is a clear sign of phase transition: With increasing system size the GMFEs tend to opposite directions on both sides of their crossing point. Note that there is no well-defined crossing point due to the irrelevant term in Eq. (20). Applying the MFSS method described in Sec. III A with the principles of Sec. III C to the raw data leads to a well-fitting function; see red lines in Fig. 1. After the subtraction of the irrelevant part from the raw data, plotting it as a function of $\varrho L^{\frac{1}{\nu}}$ results a scaling function also; see insets of Fig. 1.

The MFSS provided us the critical point W_c, the critical exponent ν, and the irrelevant exponent y at every investigated values of q; the results are given in Fig. 2. The parameters of the critical point correspond to the system itself, therefore it should not depend on the quantity we used to find it. In other words, it should be independent of q, the averaging method and the GMFE we used. From Fig. 2 it is clear that this requirement is fulfilled very nicely. There is a small deviation for the irrelevant exponent y, obtained from α^{typ} at $q = -1$ and $q = -0.75$ in the unitary and symplectic class, but since y describes the subleading part, it is very hard to determine, and we cannot exclude some sort of underestimation of the error bar of this exponent. Another interesting feature of the results is that the error bars get larger as q goes above 1. As written in Sec. III C, large q enhances the errors through the qth power in Eq. (7), leading to bigger error bars. A

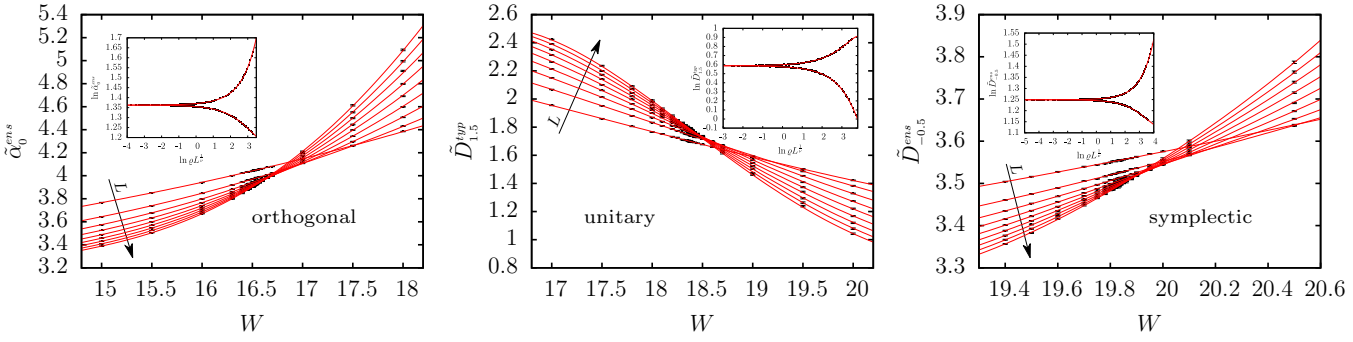

FIG. 1. (Color online) Dots are the raw data for different GMFEs in the conventional WD symmetry classes. Red line is the best fit obtained by MFSS. Insets are scaling functions on a ln-ln scale, after the irrelevant term was subtracted. Error bars are shown only on the large figures in order not to overcomplicate the insets.

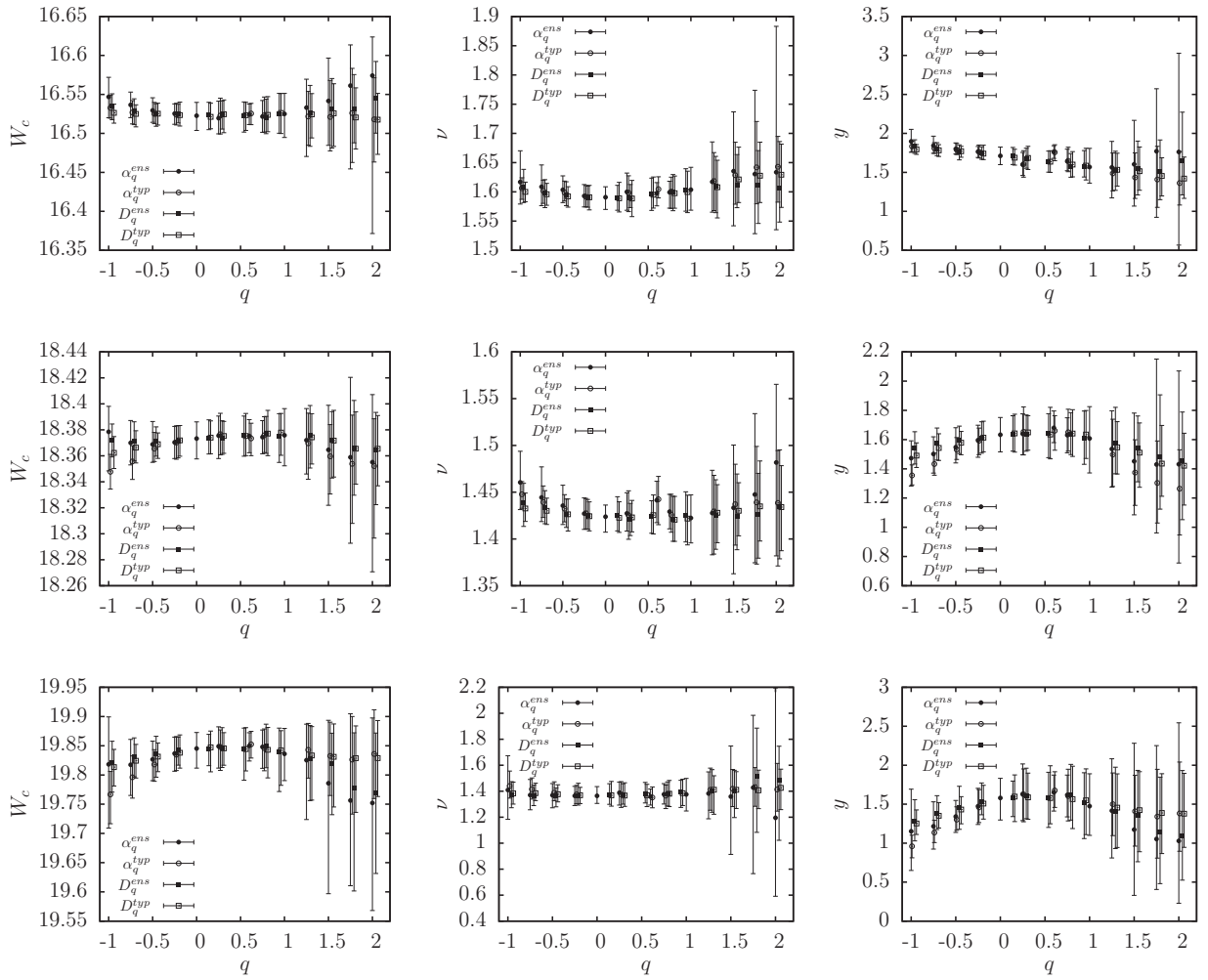

FIG. 2. Critical parameters of the Anderson models in WD classes obtained by MFS at fixed $\lambda = 0.1$. First row corresponds to the orthogonal class, second row corresponds to the unitary class, and third row corresponds to the symplectic class.

similar effect can be seen around $q \approx -1$, where the relatively less precise small wave-function values dominate the sums in Eq. (7), which can also contribute to the deviation of y obtained from $\tilde{\alpha}^{\text{typ}}$ in this regime. These two effects together lead to our investigated interval $-1 \leqslant q \leqslant 2$, where GMFEs behave the best. The results are strongly correlated, since they were obtained from the same wave functions, therefore they cannot be averaged. We chose a typical q point for every symmetry class to describe the values of the critical parameters; see Table II.

In the orthogonal class the critical parameters are in excellent agreement with the most recent high-precision results of Rodriguez *et al.* [14], $W_{c\,\text{Rod}}^{O\lambda} = 16.517$ (16.498..16.533), $\nu_{\text{Rod}}^{O\lambda} = 1.612$ (1.593..1.631), and $y_{\text{Rod}}^{O\lambda} = 1.67$ (1.53..1.80), obtained from $\tilde{\alpha}_0$ with the same method (fixed λ). This agreement verifies our numerics and fit method, and makes it reliable for the other two universality classes.

In the unitary class the critical parameters match with the results of Slevin and Ohtsuki [15], $W_{c\,\text{Sle}}^{U} = 18.375$ (18.358..18.392) and $\nu_{\text{Sle}}^{U} = 1.43$ (1.37..1.49), obtained by transfer matrix method (they did not published the value of the irrelevant exponent). They used a magnetic flux $\Phi = \frac{1}{4}$, while we used $\Phi = \frac{1}{5}$ and, according to Dröse *et al.* [23], W_c^U depends on the applied magnetic flux. However, in Fig. 2. of Ref. [23] it can be seen that the critical points at $\Phi = \frac{1}{4}$ and $\Phi = \frac{1}{5}$ are very close to each other, hence the agreement between our critical point and the result of Slevin and Ohtsuki.

In the symplectic class the critical parameters agree more or less with the results of Asada *et al.* [16], $W_{c\,\text{Asa}}^{S} =$

TABLE II. Result of the MFSS at fixed $\lambda = 0.1$ for the selected values of q.

Class	Exponent	W_c^λ	ν^λ	y^λ	N_{df}	χ^2	$n_r n_{ir} n_\varrho n_\eta$
Ort	$\tilde{\alpha}_{0.6}^{\text{ens}}$	16.524 (16.511..16.538)	1.598 (1.576..1.616)	1.763 (1.679..1.842)	172	176	3 2 1 0
Uni	$\tilde{\alpha}_{0}^{\text{ens/typ}}$	18.373 (18.358..18.386)	1.424 (1.407..1.436)	1.633 (1.516..1.751)	198	179	4 2 1 0
Sym	$\tilde{D}_{-0.25}^{\text{typ}}$	19.838 (19.812..19.869)	1.369 (1.305..1.430)	1.508 (1.309..1.743)	171	151	4 2 1 0

20.001 (19.984..20.018), $\nu^S_{\text{Asa}} = 1.375$ (1.359..1.391), and $y^S_{\text{Asa}} = 2.5$ (1.7..3.3), obtained by transfer matrix method. However, the difference does not seem to be very large: our critical point is considerably different, even though we used exactly the same model. Due to bigger computational resources we could investigate much bigger system sizes than they did, therefore it is possible that they underestimated the role of the irrelevant scaling, resulting in a somewhat higher critical point.

The critical points are higher in the unitary and in the symplectic class than in the orthogonal class, showing that broken time-reversal or spin-rotational symmetry requires more disorder to localize wave functions. Since the value of the critical point in the unitary and symplectic class can be influenced by the strength of the applied magnetic flux and spin-orbit coupling, the relationship between $W_c^{U\lambda}$ and $W_c^{S\lambda}$ probably depends on these two parameters. However, because of their close value of the critical exponents, $\nu^{U\lambda}$ and $\nu^{S\lambda}$ are the same within our confidence interval, and the following relation appears: $\nu^{O\lambda} > \nu^{U\lambda} \geqslant \nu^{S\lambda}$. The situation for the irrelevant exponent is similar; namely, they are the same within error bar, but $y^{O\lambda}$ seems to be slightly higher than $y^{U\lambda}$, which is a bit higher than $y^{S\lambda}$.

B. Results of the multifractal finite-size scaling at varying λ

As mentioned in Sec. III C, GMFEs obtained by *typical* averaging are equal to *ensemble*-averaged GMFEs only in a range of q, $q_- < q < q_+$. Since we intend to compute the MFEs also, we restrict our analysis to *ensemble* averaged GMFEs, and drop the label *ens* from the notation.

We fit the formula (24) to the raw data. To do that, we choose a range of box size ℓ, which is used for the MFSS. We always use the widest range of ℓ that results in convergence: $\chi^2/(N_{df} - 1) \approx 1$. We find that for our dataset and for different values of q for α_q or D_q, different ranges of ℓ were the best. We used minimal box sizes $\ell_{\min} = 2$ or $\ell_{\min} = 3$ and maximal box sizes corresponding to $\lambda_{\max} = 0.1$ or $\lambda_{\max} = 0.066$. At $\alpha_{0.4}$ and $\alpha_{0.6}$ the fitting method sometimes suffered from convergence troubles and resulted in large error bars, because these points are close to the special case of $q = 0.5$ where, by definition, $\alpha_{0.5} = d$. Artifacts from this regime were also reported in Ref. [14], so we decided not to take into account these points for α. We tried several combinations of $\ell_{\min}$, $\lambda_{\max}$ and expansion orders in the *symplectic* class for $\alpha_{1.75}$ and α_2, but none of them resulted in stable fit parameters. Therefore, values computed from these points are also missing from our final results, which are visible

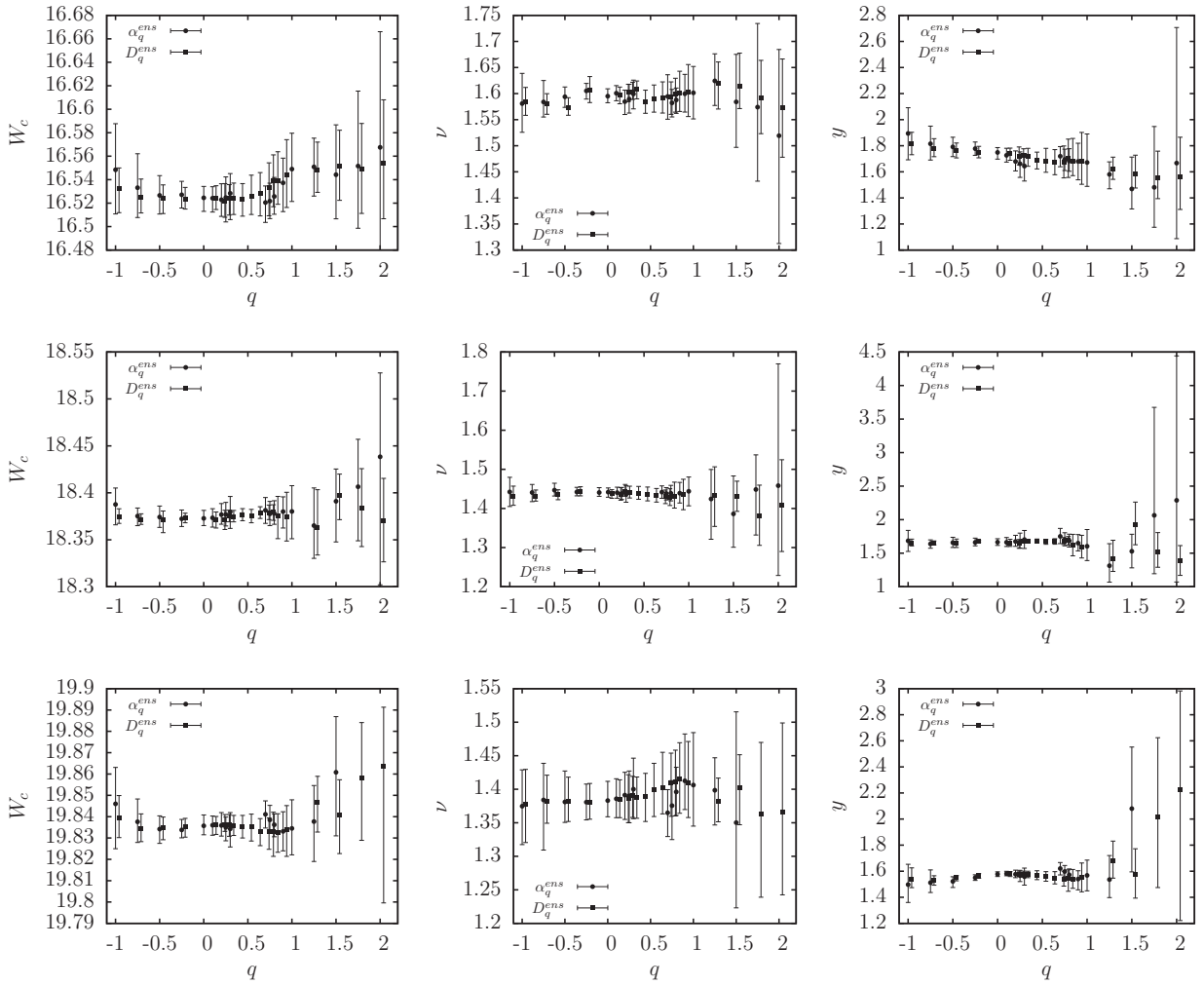

FIG. 3. Critical parameters of the Anderson models in WD classes obtained by two-variable MFFS with varying λ. First row corresponds to the orthogonal class, second row corresponds to the unitary class, and third row corresponds to the symplectic class.

TABLE III. Critical parameters of the Anderson models in the WD symmetry classes obtained by two-variable MFSS with varying λ.

Class	Exponent	W_c	ν	y	N_{df}	χ^2	$n_r n_{ir} n_\varrho n_\eta$
Ort	$\tilde{\alpha}_0$	16.524 (16.513..16.534)	1.595 (1.582..1.609)	1.749 (1.697..1.786)	241	267	3 2 1 0
Uni	$\tilde{D}_{0.1}$	18.371 (18.363..18.380)	1.437 (1.426..1.448)	1.651 (1.601..1.707)	275	232	4 2 1 0
Sym	$\tilde{\alpha}_0$	19.836 (19.831..19.841)	1.383 (1.359..1.412)	1.577 (1.559..1.595)	361	352	3 2 1 0

in Fig. 3. The results are independent of q and the GMFE we used, similar to the fixed-λ method. In Sec. IV A we already saw that, according to the arguments of Sec. III C, error bars get bigger if q grows beyond 1. This phenomenon is more amplified here, especially for values coming from fits for α_q, but larger error bars on values corresponding to D_q are present on a moderate level also. Since Fig. 8 of Ref. [14] shows results for this regime only for values corresponding to Δ_q, which is a linear transform of D_q, we can compare their results only to ours corresponding to D_q. One can see that our error bars are similar, even though there are differences probably due to the fact that they used system sizes up to $L = 120$, which was not possible for us, mainly because of the long runtime and large memory usage for the symplectic model. They also use $\ell_{\min} = 1$ and $\ell_{\min} = 2$, while $\ell_{\min} = 1$ was never suitable for our dataset. We do not know the precise origin of this behavior, but we have a few possible explanations. We experience that larger system sizes allow a wider range of ℓ to be used. We have smaller system sizes than Ref. [14], and fewer samples for the largest systems sizes. Noise also gets bigger as ℓ decreases, because of the smoothing effect of boxing described in Sec. III C, which can also explain partly our experience. Another important difference is that in Eq. (37) of Ref. [14], the authors use an expression in the expansion of the scaling function, which is proportional to the square of the irrelevant term, $(\eta\ell^{-y})^2$. According to our experience the inclusion of this term produced no improvement in the scaling analysis, so we used the scaling function described in Eq. (24). Such a difference might be explained again by our different dataset.

As written in Sec. IV A, the results for different values of q are strongly correlated, therefore we chose one of them with the lowest error bars that represents well the results for that universality class.

The critical parameters listed in Table III are in a very nice agreement with our previous results for the fixed method of $\lambda = 0.1$, see Sec. IV A, and also with the results of Refs. [14–16]. Comparing the critical parameters for the orthogonal case with the results of Rodriguez *et al.* [14] obtained by the same method, $W_{c\,\mathrm{Rod}}^{O} = 16.530$ (16.524..16.536), $\nu_{\mathrm{Rod}}^{O} = 1.590$ (1.579..1.602), we see a nice agreement again. Moreover, these results are more accurate with this method compared to the fixed λ method, leading to (for y^O and y^U only, almost) significantly different critical exponents and irrelevant exponents for the different WD classes, $\nu^O > \nu^U > \nu^S$ and $y^O \geqslant y^U > y^S$.

C. Analysis of multifractal exponents

MFSS for varying λ provided us the MFEs in all WD classes, which are listed in Table IV, and depicted in Fig. 4. For the orthogonal class one can find matching results with the listed MFEs in Ref. [14]. Since the precise values of the MFEs in three dimensions were determined first in Ref. [14] for the orthogonal class only, the lack of reliable analytical and numerical results for the other symmetry classes makes our results more important. The most conspicuous thing in Fig. 4 is that curves for different symmetry classes are very close to each other; they are almost indistinguishable at the first sight. This shows that the broken time-reversal or spin

TABLE IV. MFE α_q, D_q, and $f(\alpha_q)$, and values for the corresponding symmetry relation Eq. (11) obtained for the WD symmetry classes.

q	Class	α_q	D_q	$f(\alpha_q)$	$\alpha_q + \alpha_{1-q}$	$\Delta_q - \Delta_{1-q}$
−1	Ort	5.555 (5.490..5.626)	3.926 (3.914..3.938)	2.297 (2.338..2.250)	6.275 (6.042..6.661)	− 0.102 (−0.218..0.000)
−1	Uni	5.671 (5.629..5.707)	3.970 (3.966..3.976)	2.269 (2.303..2.245)	6.331 (6.215..6.444)	− 0.130 (−0.195.. − 0.062)
−1	Sym	5.751 (5.690..5.799)	4.001 (3.994..4.010)	2.251 (2.298..2.222)	6.379 (6.197..6.584)	− 0.134 (−0.237.. − 0.063)
−0.75	Ort	5.225 (5.187..5.267)	3.715 (3.708..3.722)	2.582 (2.599..2.564)	6.153 (5.988..6.353)	− 0.035 (−0.094..0.032)
−0.75	Uni	5.333 (5.317..5.349)	3.751 (3.749..3.754)	2.565 (2.573..2.557)	6.176 (6.131..6.239)	− 0.062 (−0.098.. − 0.025)
−0.75	Sym	5.406 (5.387..5.430)	3.773 (3.770..3.777)	2.549 (2.558..2.537)	6.221 (6.113..6.349)	− 0.060 (−0.114.. − 0.023)
−0.5	Ort	4.876 (4.856..4.896)	3.492 (3.488..3.496)	2.800 (2.803..2.796)	6.061 (5.959..6.149)	− 0.008 (−0.045..0.025)
−0.5	Uni	4.975 (4.958..4.994)	3.517 (3.512..3.521)	2.788 (2.789..2.785)	6.103 (6.000..6.167)	− 0.009 (−0.025..0.004)
−0.5	Sym	5.030 (5.019..5.039)	3.532 (3.531..3.534)	2.784 (2.787..2.781)	6.103 (6.039..6.206)	− 0.019 (−0.041.. − 0.001)
−0.25	Ort	4.488 (4.477..4.499)	3.254 (3.252..3.255)	2.945 (2.946..2.944)	6.016 (5.951..6.094)	0.000 (−0.012..0.010)
−0.25	Uni	4.563 (4.553..4.574)	3.267 (3.266..3.268)	2.943 (2.945..2.941)	6.037 (5.998..6.081)	− 0.006 (−0.011..0.002)
−0.25	Sym	4.607 (4.603..4.611)	3.274 (3.274..3.275)	2.941 (2.941..2.941)	6.033 (5.997..6.072)	− 0.004 (−0.011..0.003)
0	Ort	4.043 (4.035..4.049)	3 (3..3)	3 (3..3)	5.991 (5.965..6.012)	0 (0..0)
0	Uni	4.094 (4.087..4.101)	3 (3..3)	3 (3..3)	6.000 (5.974..6.026)	0 (0..0)
0	Sym	4.124 (4.121..4.127)	3 (3..3)	3 (3..3)	6.010 (5.999..6.023)	0 (0..0)
0.1	Ort	3.849 (3.843..3.855)	2.895 (2.894..2.895)	2.990 (2.989..2.991)	5.995 (5.978..6.014)	− 0.001 (−0.003..0.002)
0.1	Uni	3.890 (3.883..3.897)	2.890 (2.889..2.891)	2.990 (2.988..2.991)	5.997 (5.981..6.014)	0.000 (−0.002..0.002)

TABLE IV. *(Continued.)*

q	Class	α_q	D_q	$f(\alpha_q)$	$\alpha_q + \alpha_{1-q}$	$\Delta_q - \Delta_{1-q}$
0.1	Sym	3.913 (3.911..3.915)	2.887 (2.886..2.887)	2.989 (2.989..2.990)	6.005 (5.998..6.013)	0.001 (−0.000..0.002)
0.2	Ort	3.645 (3.638..3.651)	2.789 (2.786..2.790)	2.960 (2.957..2.962)	5.998 (5.985..6.011)	−0.001 (−0.005..0.003)
0.2	Uni	3.678 (3.673..3.684)	2.778 (2.777..2.780)	2.958 (2.956..2.961)	5.999 (5.987..6.011)	−0.000 (−0.004..0.004)
0.2	Sym	3.693 (3.691..3.695)	2.772 (2.772..2.773)	2.956 (2.955..2.957)	5.999 (5.995..6.004)	0.001 (−0.000..0.003)
0.25	Ort	3.541 (3.534..3.547)	2.734 (2.733..2.737)	2.936 (2.933..2.939)	6.000 (5.987..6.012)	−0.001 (−0.006..0.003)
0.25	Uni	3.569 (3.563..3.575)	2.721 (2.720..2.722)	2.933 (2.931..2.935)	5.999 (5.987..6.011)	−0.000 (−0.002..0.001)
0.25	Sym	3.579 (3.577..3.581)	2.715 (2.714..2.715)	2.931 (2.930..2.932)	5.997 (5.992..6.001)	0.001 (−0.001..0.003)
0.3	Ort	3.436 (3.430..3.441)	2.681 (2.678..2.684)	2.907 (2.903..2.911)	6.001 (5.991..6.012)	−0.001 (−0.006..0.004)
0.3	Uni	3.459 (3.453..3.464)	2.665 (2.664..2.666)	2.903 (2.900..2.905)	5.999 (5.987..6.010)	−0.000 (−0.002..0.001)
0.3	Sym	3.465 (3.462..3.467)	2.657 (2.656..2.658)	2.899 (2.898..2.901)	5.995 (5.991..6.000)	0.001 (−0.001..0.003)
0.4	Ort		2.573 (2.570..2.577)			−0.001 (−0.006..0.004)
0.4	Uni		2.551 (2.550..2.553)			−0.000 (−0.002..0.002)
0.4	Sym		2.542 (2.540..2.543)			0.001 (−0.001..0.003)
0.5	Ort	3 (3..3)	2.466 (2.459..2.471)	2.733 (2.730..2.736)	6 (6..6)	0 (0..0)
0.5	Uni	3 (3..3)	2.439 (2.437..2.441)	2.719 (2.719..2.721)	6 (6..6)	0 (0..0)
0.5	Sym	3 (3..3)	2.427 (2.425..2.429)	2.714 (2.712..2.715)	6 (6..6)	0 (0..0)
0.6	Ort		2.358 (2.352..2.366)			0.001 (−0.004..0.006)
0.6	Uni		2.327 (2.325..2.329)			0.000 (−0.002..0.002)
0.6	Sym		2.314 (2.311..2.317)			−0.001 (−0.003..0.001)
0.7	Ort	2.566 (2.561..2.571)	2.252 (2.242..2.263)	2.472 (2.466..2.479)	6.001 (5.991..6.012)	0.001 (−0.004..0.006)
0.7	Uni	2.540 (2.535..2.545)	2.217 (2.214..2.220)	2.443 (2.438..2.448)	5.999 (5.987..6.010)	0.000 (−0.001..0.002)
0.7	Sym	2.530 (2.528..2.532)	2.203 (2.199..2.207)	2.432 (2.429..2.435)	5.995 (5.991..6.000)	−0.001 (−0.003..0.001)
0.75	Ort	2.459 (2.454..2.465)	2.198 (2.186..2.209)	2.394 (2.387..2.401)	6.000 (5.987..6.012)	0.001 (−0.003..0.006)
0.75	Uni	2.430 (2.424..2.436)	2.163 (2.159..2.168)	2.363 (2.358..2.369)	5.999 (5.987..6.011)	0.000 (−0.001..0.002)
0.75	Sym	2.417 (2.415..2.419)	2.148 (2.143..2.156)	2.350 (2.347..2.353)	5.997 (5.992..6.001)	−0.001 (−0.003..0.001)
0.8	Ort	2.354 (2.347..2.360)	2.147 (2.135..2.157)	2.312 (2.304..2.319)	5.998 (5.985..6.011)	0.001 (−0.003..0.005)
0.8	Uni	2.320 (2.314..2.326)	2.111 (2.099..2.125)	2.278 (2.271..2.286)	5.999 (5.987..6.011)	0.000 (−0.004..0.004)
0.8	Sym	2.307 (2.304..2.309)	2.095 (2.090..2.100)	2.264 (2.261..2.267)	5.999 (5.995..6.004)	−0.001 (−0.003..0.000)
0.9	Ort	2.146 (2.135..2.159)	2.046 (2.029..2.060)	2.136 (2.124..2.149)	5.995 (5.978..6.014)	0.001 (−0.002..0.003)
0.9	Uni	2.107 (2.097..2.117)	2.009 (1.991..2.025)	2.097 (2.087..2.108)	5.997 (5.981..6.014)	−0.000 (−0.002..0.002)
0.9	Sym	2.092 (2.088..2.099)	1.988 (1.981..1.997)	2.082 (2.077..2.088)	6.005 (5.998..6.013)	−0.001 (−0.002..0.000)
1	Ort	1.948 (1.930..1.963)	α_1	α_1	5.991 (5.965..6.012)	0 (0..0)
1	Uni	1.905 (1.886..1.925)	α_1	α_1	6.000 (5.974..6.026)	0 (0..0)
1	Sym	1.886 (1.877..1.896)	α_1	α_1	6.010 (5.999..6.023)	0 (0..0)
1.25	Ort	1.520 (1.508..1.535)	1.727 (1.715..1.738)	1.477 (1.418..1.551)	6.009 (5.985..6.034)	−0.001 (−0.006..0.003)
1.25	Uni	1.473 (1.442..1.499)	1.688 (1.660..1.708)	1.422 (1.391..1.457)	6.036 (5.995..6.073)	0.006 (−0.002..0.011)
1.25	Sym	1.437 (1.424..1.450)	1.644 (1.634..1.655)	1.371 (1.338..1.409)	6.044 (6.027..6.061)	0.004 (0.001..0.007)
1.5	Ort	1.185 (1.161..1.206)	1.534 (1.518..1.550)	1.007 (0.912..1.079)	6.061 (6.017..6.102)	0.005 (−0.009..0.019)
1.5	Uni	1.096 (1.073..1.124)	1.468 (1.453..1.483)	0.958 (0.836..1.017)	6.072 (6.031..6.118)	0.009 (−0.004..0.025)
1.5	Sym	1.060 (1.044..1.080)	1.450 (1.437..1.465)	0.889 (0.827..1.011)	6.090 (6.063..6.118)	0.024 (0.015..0.034)
1.75	Ort	0.920 (0.889..0.949)	1.372 (1.349..1.395)	0.590 (0.422..0.818)	6.145 (6.076..6.216)	0.029 (−0.001..0.058)
1.75	Uni	0.841 (0.814..0.873)	1.301 (1.273..1.329)	0.479 (0.459..0.529)	6.175 (6.130..6.222)	0.041 (0.015..0.065)
1.75	Sym	no stability	1.262 (1.242..1.290)			0.050 (0.030..0.077)
2	Ort	0.719 (0.683..0.754)	1.231 (1.203..1.256)	0.190 (−0.068..0.727)	6.274 (6.173..6.380)	0.083 (0.031..0.132)
2	Uni	0.622 (0.583..0.690)	1.173 (1.147..1.205)	0.131 (0.039..0.230)	6.293 (6.212..6.396)	0.113 (0.076..0.154)
2	Sym	no stability	1.118 (1.099..1.167)			0.120 (0.083..0.184)

rotational symmetry has a very small effect on the MFEs in three dimensions. Taking a closer look (or from Table IV) one can see that the curve of D_q and α_q are the steepest in the symplectic class, the second steepest in the unitary class, and the less steep in the orthogonal class. From Table IV it is also clear that at most of the q values there is a significant difference between the MFEs of different symmetry classes.

There are no critical states in the two-dimensional orthogonal class [12], but one can find values of α_0 for the two-dimensional unitary class (integer quantum Hall), $\alpha^U_{02D} = 2.2596 \pm 0.0004$ [24], and symplectic class, $\alpha^S_{02D} = 2.172 \pm 0.002$ [25]. Comparing the difference between these exponents in two dimensions, we get $\alpha^U_{02D} - \alpha^S_{02D} = 0.0876 \pm 0.0024$, while our result for three dimensions is $\alpha^U_{03D} - \alpha^S_{03D} = -0.03 \pm 0.015$. There is about a factor of three between the magnitude of these values, and even their sign is opposite, which shows very a different effect of presence or absence of spin-rotational symmetry in different dimensions.

We tested the symmetry relation Eq. (11) for α_q and Δ_q, the results are listed in Table IV and depicted in Fig. 5. The

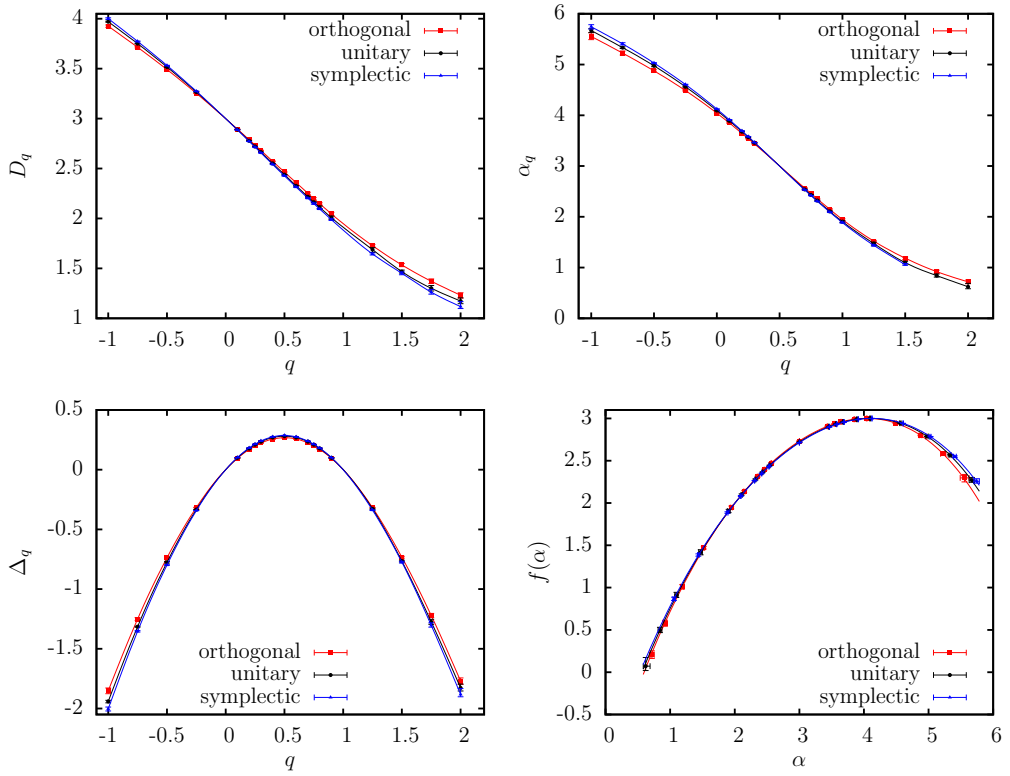

FIG. 4. (Color online) MFEs of the Anderson models in the WD universality classes. Corresponding data are listed in Table IV.

symmetry relation is fulfilled in the range $-0.25 \leqslant q \leqslant 1.25$ (in the *symplectic* class only for $-0.25 \leqslant q \leqslant 1$), and small deviations are visible outside this interval. In this regime error bars are growing very large, coming mainly from the large errors of $\alpha_{q\geqslant 1.5}$ and $D_{q\geqslant 1.5}$. Similar effects were already seen for the critical parameters in Fig. 3. It is really hard to estimate the correct error bars in this large-q case, and the deviations from symmetry are small; therefore we believe that differences appear only because of slightly underestimated error bars of $\alpha_{q\geqslant 1.5}$ and $D_{q\geqslant 1.5}$. All in all we find numerical results that basically match Eq. (11).

Assuming that Δ_q is an analytic function of q, and using the symmetry relation, Eq. (11), one can expand Δ_q in Taylor series around $q = \frac{1}{2}$:

$$\begin{aligned}\Delta_q &= \sum_{k=0}^{\infty} c_k \left(q-\frac{1}{2}\right)^{2k} = \sum_{k=0}^{\infty} c_k \left[q(q-1)+\frac{1}{4}\right]^k \\ &= \sum_{k=0}^{\infty} c_k \sum_{i=0}^{k} \binom{k}{i} [q(q-1)]^i \left(\frac{1}{4}\right)^{k-i} \\ &= \sum_{k=1}^{\infty} d_k [q(1-q)]^k, \end{aligned} \tag{30}$$

where the condition $\Delta_0 = \Delta_1 = 0$ enforced by the definition of Δ_q [see Eq. (9)] was used in the last step, leading to $k = 1$

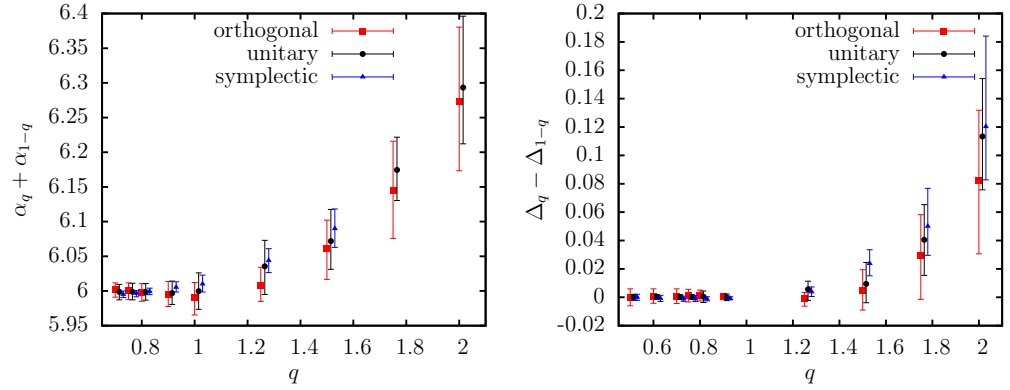

FIG. 5. (Color online) Test for symmetry relation Eq. (11) in the WD symmetry classes. Points are shifted horizontally a little bit for better visualization. Only the range $q \geqslant 0.5$ is visible because expression $\alpha_q + \alpha_{1-q}$ ($\Delta_q - \Delta_{1-q}$) is symmetric (antisymmetric) for $q = 0.5$.

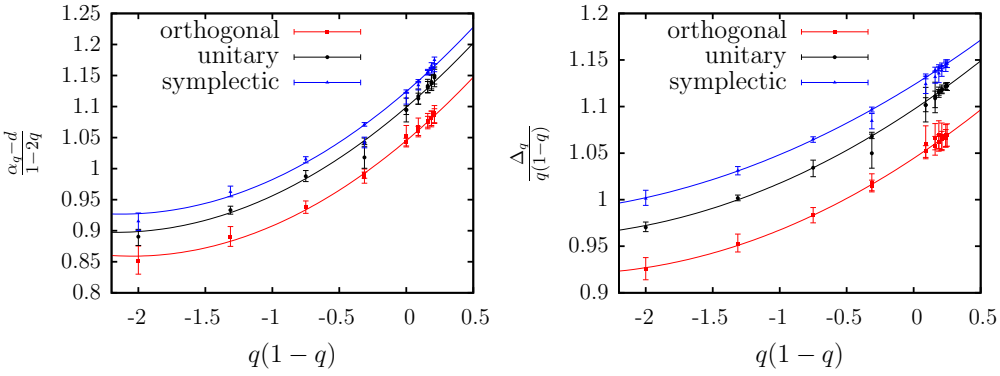

FIG. 6. (Color online) Dots and error bars are numerical values for the corresponding quantities, $\frac{\alpha(q)-d}{1-2q}$ and $\frac{\Delta(q)}{q(1-q)}$, for the WD symmetry classes. Lines are the best fits. Several points are shifted horizontally a bit for better viewing.

as the lower bound for the summation. Similar expression can be derived for α_q by using the connection $\alpha_q = d + \frac{d}{dq}\Delta_q$ derived from Eqs. (8) and (9):

$$\alpha_q = d + (1-2q)\sum_{k=1}^{\infty} a_k [q(1-q)]^{k-1}, \tag{31}$$

where $a_k = kd_k$, and $a_1 = d_1 = \alpha_0 - d$. One can obtain the d_k and a_k coefficients by fitting the expressions Eq. (30) and (31). We used only the range $q \leqslant 1.25$, because beyond this regime error bars grow extremely large, and there are small deviations from the symmetry relation (11) also. We plotted $\frac{\Delta(q)}{q(1-q)}$ and $\frac{\alpha(q)-d}{1-2q}$ in Fig. 6 to make the presence of higher-order terms of the expansion visible.

We fit expressions Eq. (30) and (31) up to third order in all cases, the resulting expansion coefficients are listed in Table V. From the data listed one can see that the expansion coefficients fulfill the relation $a_k = kd_k$. However α_q and Δ_q were obtained from the same wave functions, they are results of completely independent fit procedures. Therefore the fact that they satisfy the equation $a_k = kd_k$ further confirms our result for their value listed in Table IV for $q \leqslant 1.25$ and shows the consistency of the MFSS.

As one would expect for expansion coefficients, d_k and a_k show decreasing behavior as k grows. Only d_1 and a_1 are significantly different for the different symmetry classes, while d_2, d_3, a_2, and a_3 are the same within error bars. Their real value is probably different, but the relative error of the expansion coefficients naturally increases as k grows, leading to indistinguishable values for the different symmetry classes for $k \geqslant 2$.

Wegner computed analytically [26] the value of Δ_q with ε expansion using nonlinear σ model up to fourth-loop order for the orthogonal and the unitary symmetry class, resulting an expansion in dimensions $d = 2 + \varepsilon$ for $\varepsilon \ll 1$ [12]:

$$\begin{aligned}\Delta_q^O &= q(1-q)\varepsilon + \frac{\zeta(3)}{4}q(q-1)(q^2-q+1)\varepsilon^4 + O(\varepsilon^5)\\ &= \left(\varepsilon - \frac{\zeta(3)}{4}\varepsilon^4\right)q(1-q)\\ &\quad + \frac{\zeta(3)}{4}\varepsilon^4[q(1-q)]^2 + O(\varepsilon^5),\end{aligned} \tag{32}$$

$$\Delta_q^U = \sqrt{\frac{\varepsilon}{2}}q(1-q) - \frac{3}{8}\zeta(3)\varepsilon^2[q(1-q)]^2 + O\left(\varepsilon^{\frac{5}{2}}\right). \tag{33}$$

Even though $\varepsilon \ll 1$ should hold, one can try to extrapolate to three dimensions by inserting $\varepsilon = 1$. This leads to $d_1^O \approx 0.699$, $d_2^O \approx 0.301$, $d_1^U \approx 0.707$, and $d_2^U \approx -0.451$. As one can see, these values are rather far from our numerical results, but this is not surprising for an ε expansion at $\varepsilon = 1$. These results capture well the tendency at least that d_1^O is slightly smaller than d_1^U. On the other hand it leads to d_2^O and d_2^U having opposite signs, which is highly inconsistent with our numerical results. It is interesting that the first-loop term, which is proportional to ε and leads to parabolic Δ_q, results in $d_1^O = 1$ and $a_1^O = \alpha_0 - d = 1$, which are very close to our numerically measured values. In this sense parabolic approximation is better for the orthogonal class, as compared to the fourth-loop order approximation. If higher-order terms were obtained, or if Δ_q were expanded by using another approach, our coefficients

TABLE V. Expansion coefficients of Eqs. (30) and (31) obtained by the fit depicted in Fig. 6.

	Ort	Uni	Sym
d_1	1.044 (1.041..1.047)	1.097 (1.095..1.098)	1.123 (1.122..1.125)
d_2	0.095 (0.085..0.105)	0.096 (0.091..0.100)	0.088 (0.084..0.093)
d_3	0.018 (0.011..0.025)	0.017 (0.014..0.020)	0.014 (0.010..0.017)
a_1	1.045 (1.042..1.048)	1.099 (1.096..1.102)	1.124 (1.123..1.126)
a_2	0.182 (0.168..0.195)	0.185 (0.174..0.197)	0.185 (0.179..0.191)
a_3	0.044 (0.035..0.053)	0.043 (0.035..0.050)	0.044 (0.038..0.049)

could provide relatively accurate values as compared with analytical results.

V. SUMMARY

In this paper we examined the three-dimensional Anderson models belonging to the conventional WD symmetry classes with the help of multifractal finite-size scaling using two methods: a simpler method for fixed λ leading to a single-variable scaling function, and a more complicated one for varying λ, resulting in a two-variable scaling function. Both methods confirmed the presence of multifractality in all three symmetry classes, and we obtained critical parameters listed in Tables II and III in agreement with each other and with previous results known from the literature. The more complicated varying-λ method provided more precise values for the critical parameters, as listed in Table III, and significantly different critical exponents for the different WD symmetry classes.

Applying the method of varying λ we also calculated the multifractal exponents that basically fulfill the expected symmetry relation Eq. (11), small deviations were detected for large q values probably due to slightly underestimated error bars. In Fig. 4 one can see that the MFEs of different symmetry classes are very close to each other, but Fig. 6 or Table IV shows significant differences between them for most of the values of q. We compared the difference of α_0 in the unitary and symplectic class to available results in two dimensions and found completely different relations between the two- and three-dimensional cases. We expanded the MFEs in terms of the variable $q(1-q)$, and determined the expansion coefficients up to third order numerically. The expansion coefficients of Eqs. (30) and (31) fulfill the expected relation $a_k = kd_k$ giving a further confirmation for the validity of our results for the MFEs listed in Table IV. We also compared the numerical results to available analytical estimates, and found in some cases similar, but in other cases opposite, qualitative behavior for expansion coefficients for the orthogonal and the unitary classes. Nevertheless, we believe that the numerical precision of our results should be used as tests for future renormalization or other type of expansion approximations. Therefore, our results await analytical comparison.

ACKNOWLEDGMENT

Financial support from OTKA under Grant No. K108676 and the Alexander von Humboldt Foundation is gratefully acknowledged.

[1] P. W. Anderson, Phys. Rev. **109**, 1492 (1958).
[2] H. Hu, A. Strybulevych, J. H. Page, S. E. Skipetrov, and B. A. van Tiggelen, Nat. Phys. **4**, 945 (2008).
[3] S. Faez, A. Strybulevych, J. H. Page, and A. Lagendijk, Phys. Rev. Lett. **103**, 155703 (2009).
[4] M. Segev, Y. Silberberg, and D. N. Christodoulides, Nat. Photonics **7**, 197 (2013).
[5] F. Jendrzejewski, A. Bernard, K. Müller, P. Cheinet, V. Josse, M. Piraud, L. Pezz, L. Sanchez-Palencia, A. Aspect, and P. Bouyer, Nat. Phys. **8**, 398 (2012).
[6] A. Richardella, P. Roushan, S. Mack, B. Zhou, D. A. Huse, D. D. Awschalom, and A. Yazdani, Science **327**, 665 (2010).
[7] H. Aoki and T. Ando, Solid State Commun. **38**, 1079 (1981).
[8] M. V. Feigelman, L. B. Ioffe, V. E. Kravtsov, and E. Cuevas, Ann. Phys. (NY) **325**, 1390 (2010); I. S. Burmistrov, I. V. Gornyi, and A. D. Mirlin, Phys. Rev. Lett. **108**, 017002 (2012).
[9] S. Kettemann, E. R. Mucciolo, I. Varga, and K. Slevin, Phys. Rev. B **85**, 115112 (2012); S. Kettemann, E. R. Mucciolo, and I. Varga, Phys. Rev. Lett. **103**, 126401 (2009).
[10] M. Giordano, T. G. Kovács, and F. Pittler, Phys. Rev. Lett. **112**, 102002 (2014).
[11] M. Giordano, T. G. Kovács, F. Pittler, L. Ujfalusi, and I. Varga, PoS LATTICE **2014**, 212 (2015).
[12] F. Evers and A. D. Mirlin, Rev. Mod. Phys. **80**, 1355 (2008).
[13] I. Varga, E. Hofstetter, and J. Pipek, Phys. Rev. Lett. **82**, 4683 (1999).
[14] A. Rodriguez, L. J. Vasquez, K. Slevin, and R. A. Römer, Phys. Rev. B **84**, 134209 (2011).
[15] K. Slevin and T. Ohtsuki, Phys. Rev. Lett. **78**, 4083 (1997).
[16] Y. Asada, K. Slevin, and T. Ohtsuki, J. Phys. Soc. Jpn. **74**, 238 (2005).
[17] O. Schenk, M. Bollhöfer, and R. A. Römer, SIAM Rev. **50**, 91 (2008).
[18] A. Stathopoulos and J. R. McCombs, ACM Trans. Math. Software **37**, 21:1 (2010).
[19] L. Ujfalusi and I. Varga, Phys. Rev. B **90**, 174203 (2014).
[20] A. D. Mirlin, Y. V. Fyodorov, A. Mildenberger, and F. Evers, Phys. Rev. Lett. **97**, 046803 (2006).
[21] M. Janssen, *Fluctuations and Localization in Mesoscopic Electron Systems*, Lecture Notes in Physics, Vol 64 (World Scientific, Singapore, 2001); Phys. Rep. **295**, 1 (1998).
[22] F. James and M. Roos, Comput. Phys. Commun. **10**, 343 (1975).
[23] T. Dröse, M. Batsch, I. K. Zharekeshev, and B. Kramer, Phys. Rev. B **57**, 37 (1998).
[24] F. Evers, A. Mildenberger, and A. D. Mirlin, Phys. Rev. Lett. **101**, 116803 (2008).
[25] A. Mildenberger and F. Evers, Phys. Rev. B **75**, 041303(R) (2007).
[26] F. Wegner, Nucl. Phys. B **280**, 210 (1987).